Enhanced Anticorrosion of Nitrogen ions modified polyvinyl alcohol/Mg-Ag ions co-incorporated calcium phosphate coatings

K. Thanigai Arul[1,3,9*], E. Manikandan[2,8], J. Ramana Ramya[3,4], K. Indira[5], U. Kamachi Mudali[6], M. Henini[7], K. Asokan[9], Chung-Li Dong[10] & S. Narayana Kalkura[3]

[1]Energy and Biophotonic Laboratory, Department of Physics, AMET (Deemed to be University), Kanathur, Chennai- 603 112, Tamil Nadu, India

[2]UNESCO-UNISA Africa Chair in Nanosciences-Nanotechnology, College of Graduate Studies, University of South Africa, Muckleneuk Ridge, PO Box 392, Pretoria, South Africa

[3]Crystal Growth Centre, Anna University, Chennai-600025, India

[4]National Centre for Nanoscience and Nanotechnology, University of Madras, Guindy Campus, Chennai 600 025, Tamil Nadu, India

[5]Corrosion Science and Technology Division, Indira Gandhi Centre for Atomic Research, Kalpakkam, Tamil Nadu, India

[6]Heavy Water Board, Anushakthi Nagar, Mumbai, 400 094, India

[7]School of Physics and Astronomy, University of Nottingham, Nottingham NG7 2RD, United Kingdom (UK)

[8]Dept of Physics, Thiruvalluvar University College of Arts and Science, Thiruvalluvar University, Thennangur Village 604408, Vellore, India

[9]Inter-University Accelerator Centre, Aruna Asaf Ali Marg, New Delhi 110 067, India

[10]Department of Physics, Tamkang University, Tamsui, 25137, Taiwan

ABSTRACT

Nitrogen ions (70 keV) were implanted on composite coatings containing polymer/Mg (magnesium)–Ag (silver) ions co-incorporated hydroxyapatite which is developed by microwave irradiation. Average crystallite size of modified coatings is reduced to 80% compared to pristine. The variation of bond strength of modified coatings is realized. The electrical resistance (77%), microhardness (4.3%), roughness (4.5 times) and pore size are enhanced on the modified coatings. Superhydrophilic surface is tuned to hydrophobic on implantation. At higher fluence (1×10^{17} ions/cm^2) depicted an enhanced corrosion potential compared to the other coatings. Thus, the new insight of modified coatings is realized by correlating phase-structure, surface and anticorrosion.

Keywords: Ceramic; Composites; Coating; Surface; Corrosion

***Corresponding Author. E-mail address:thanigaiarul.k@gmail.com (K.T.A)

1.Introduction

Metals have been employed as orthopedic implants owing to their better mechanical strength. However, when they are in contact with the body fluid, toxic ions were released that could damage the surrounding tissues [1, 2]. Moreover, the metals are not bioactive and possess a weak adhesive strength with nearby tissues. In order to address this, bioceramics such as hydroxyapatite (HAp) has been used for coating on metallic substrates to improve the growth of bone at prosthetic boundary. Biocompatible of HAp is analogous to human bone composition and structure reported by Capello et al. which has weak resorbable [3-5]. Various techniques have been employed for the HAp coating onto the metallic substrates such as sol-gel [6], pulsed laser deposition [7], electrochemical deposition [8], biomimetic [9], plasma spraying [10, 11], electrophoretic deposition [12-14], ion beam sputtering [15], cold isostatic pressing [16], laser engineered net shaping [17] and electron beam evaporation [18]. In this work, microwave assisted technique is developed for coatings. It is one of the effective routes to offer many advantages such as low cost, process simplicity, and simultaneous usage of multi-substrates for uniform depositions.

Generally, the bond strength of bioactive coating with the metallic substrate was weak [19-20] and can be improved by sintering process [21]. However, the sintering at high temperatures deteriorated the HAp coating adhesion and partially converted to tricalcium phosphate (TCP) which easily dissolves in bodily fluids. In order to improve the HAp adhesion, polymeric binders can be used. A synthetic water-soluble polymer (polyvinyl alcohol) can be used as a binder with HAp to act as crystallization promoters. Further, the polymeric additives provide a good adhesion to the substrate which retaining the bioactivity [22-23].

Biocompatible metal ions have been used for a rapid bone growth which aiding to reduce infection. The metal ions such as magnesium, sodium, fluoride, strontium, zinc, iron, copper,

etc., are present in human bone [24, 25]. Apart from them, the magnesium ions play a vital role in stimulating osteoblast proliferation; its deficiency causes bone brittleness, and bone loss [26]. Recently, post-surgery and treatments have been augmented due to the growth of microorganism to decrease the bone growth rate. In order to address the significant impact, antimicrobial agents [27] can be utilized to resist the microbial growth on coatings. Silver is one of the well known antimicrobial metal ions [28]. Here, the silver ions are employed with magnesium ions to provide multi-functions which granting advanced coatings.

Even though, the coatings have rapid bone growth rates and resistant to microbes however, another major issue of the coatings is biocorrosion nowadays. Since, the corrosion is associated with the surface phenomenon in which bodily fluid interacts with the coating surface. Further, it leads to a rapid or slow leaching on the surface of coating depending on the ionic interactions. In order to sort out this issue, the surface of coating should be tuned or modified for optimized degradation rate thereby; the corrosion rate can be controlled to improve cell proliferation. Different techniques have been utilized to modify the surface of the implants viz., micro-arc oxidation [29], plasma-based low-energy ion implanted [30], laser [31], ion beam and laser processing [32], double-glow plasma [33], ion beam [34] chemical etching [35], microwave [36], etc. In this work, the low energy surface modification is used to control the structure, phase and bonding which facilitating to enhance the corrosion resistance and mechanical strength. Further, it also depends upon the chemical effects of the implanted ions, energy, ion fluence rate and localized heating during the implantation [37-39]. It only modifies the surface and not affecting the underlying bulk properties of the material. Besides, it tailors other surface properties of the coatings such as surface roughness, surface charge/energy, pores and wettability which play a crucial role to the corrosion resistance.

Nitrogen and argon ions were implanted on HAp coatings to enhance the mechanical strength [40]. Ion beam mixing technique has been used to improve the HAp adhesion on

titanium substrate [41]. Cell adhesion, bioactivity, and wettability of the biomaterials were improved by irradiation [42] and ion beam [43]. Enhanced vascularisation, cell growth, protein adsorption, mechanical strength, and corrosion resistance were attained due to the accumulation of surface defects and ballistic effect of nitrogen ions [44]. Moreover, the mechanism of enhanced corrosion resistance of materials by ion implantation is not yet explored clearly. In the present work, the effects of nitrogen ion implantation on polymer encapsulated magnesium and silver ions co-incorporated HAp nanocomposite coatings are examined. Further, the new insight into the coexistence of crystalline-partial amorphous, disorder, vacancies and new bond formation are correlated to corrosion resistance of the coatings. By varying ion fluences, how it creates oxygen vacancies, localization and delocalization of electrons are responsible for a superior anticorrosion discussed. To the best of our knowledge, there is no detailed new insight into the surface-modified coatings. It provides to develop next generation anticorrosion materials with best performance.

2. Experimental methods

2.1. Methods and Materials

The wet chemical route was employed to synthesize Mg-Ag ions co-incorporated HAp using AR grade reagents (Merck). The solution of diammonium hydrogen phosphate (0.6 M) was synthesized using the triple distilled water. Further, the solution of calcium nitrate tetrahydrate (1.0 M) was mixed with magnesium nitrate hexahydrate (0.1 M) and silver nitrate (0.1 M). Eventually, it was added to the diammonium hydrogen phosphate and ammonia solution was used to adjust pH to 10 which mixed for 2 h. Then, the solution was irradiated by microwave (900 W) for 30 minutes and dried at 80°C (oven) and denoted as MgAgHAp.

Titanium substrates (10 mm×10 mm×1 mm) were employed for coating. Then, the MgAgHAp (0.5 gram) was mixed to polymer (PVA) (0.2 gram) for preparing the polymer based nanocomposite. This solution was irradiated by microwave with metal plates for 2 min.

Subsequently, the coatings were dried in an oven at 60°C. This forms as a pristine sample of modified HAp (MgAgHAp) and labeled as p-mHAp. Using 150 kV Accelerator (AMSS, MSG, IGCAR, Kalpakkam, Tamil Nadu, India), nitrogen ions (N^+) (70 keV) were implanted on the coatings with varying ion fluences 1×10^{16}, 5×10^{16}, 1×10^{17} and 2.5×10^{17} ions/cm^2 attributed as 116-mHAp, 516-mHAp, 117-mHAp and 2517-mHAp respectively. The ion beam current was in the range 350-400 nA monitored during ion collisions and their range 302 nm calculated by a software SRIM-2008 (SRIM and TRIM, http://www.srim.org).

2.2. Characterization

GIXRD (Glazing Incidence X-ray Diffraction) was performed on the coatings using a STOE diffractometer using CuK_α (λ=0.1540 nm) and its maximum operating voltage (40KV). Atomic Force Microscopy (AFM, NT-MDT-SOLVER PRO EC system) was employed to analyze the surface morphology of samples. Two probes are used to measure the electrical resistance of coatings. The morphology of samples was examined with a Carl Zeiss MA 15/EVO 18 Scanning Electron Microscope (SEM). Using scotch tape route (ASTM D 3359-02), the coating adhesion was assessed. The surface of coating was qualitatively examined under an optical stereo microscope for assessing the adhesive strength of coating to titanium. The mechanical strength of coatings was analyzed using micro hardness tester (QV-1000DAT) and calculated using Vickers hardness formula,

$$\mathrm{HV} = 0.1891 \times \frac{F}{d^2} \text{ ---------- (1)}$$

Where, F and d are the applied load (10 g, 20 g, 30 g, 40 g and 50 g) and the average of the two diagonals of the imprint on the coating respectively. Contact angle meter (OCA 15EC, Germany) was used to measure the water contact angle using dose volume (10 mL) at 1 mL/s. Immersion test is carried out on all coatings using Phosphate Buffer Solution (PBS) for 24 hours and 96 hours. The PBS was prepared using following chemicals NaCl (8 g), KCl (0.2 g), Na_2HPO_4 (1.44 g), KH_2PO_4 (0.24 g) in 1 L deionized water [45]

The chemicals such as sodium chloride, potassium chloride, calcium chloride, sodium bicarbonate, disodium phosphate, magnesium chloride hexahydrate, potassium dihydrogen phosphate, magnesium sulfate heptahydrate and glucose were dissolved in 1 liter double-distilled water at 37°C and maintaining pH (7.4) for preparing Hank's solution. Electrochemical measurements were carried out by three-electrodes at 37°C. A silver/silver chloride was employed as a reference electrode; a platinum sheet and the test specimen (titanium) were employed as a counter and working electrode respectively. Potentiodynamic polarization experiments were performed in the Hank's solution by Solartron 1287 on the pristine and surface modified coatings at a scan rate of 10 mV min^{-1} in aerated condition. The experiments were repeated thrice in the Hank's solution for reliability. The corrosion current density (I_{corr}) and potential (E_{corr}) of the coatings were obtained from polarization curves. Electrochemical Impedance Spectroscopy (EIS) were performed using Solartron 1255.

3.Results and discussions

The ion interaction on polymer-based nanocomposite coatings causes an electronic energy loss (1.412 keV/nm) and nuclear energy loss (0.482 keV/nm). The losses were calculated using the SRIM-2008 program. The electronic energy loss was high compared to the nuclear energy loss illustrating high electronic contributions to decrease electronic density, local bonding and coordination. Further, the various ion fluences tailor defects, poor/rich oxygen vacancies, and disorders and altering the surface properties of nanocomposite coatings without depriving bulk. The coating surface was passivated by forming chemical bonds alter with respect to ion fluences.

3.1. GIXRD Analysis

GIXRD patterns of the unmodified and surface modified coatings (Fig.1) and the formed phase is matched well with the JCPDS of HAp (09-0432). MAUD (Materials Analysis Using Diffraction, http://www.ing.unitn.it/~maud/) software was employed to calculate average crystallite size and lattice parameters in Table 1. As the ion fluence increases, the crystallite

size was reduced drastically (Table 1). The crystallite size of surface-modified coating is reduced by 80 % at 2517-mHAp compared to pristine due to a high disorder and defects. On implantation, the XRD patterns confirmed the variation of crystallinity. At low fluence (116-mHAp), a high partial amorphization is observed in XRD pattern due to localized heating generated by ion solid interaction. The prominent plane (211) of 116-mHAp is reduced; however the other plane (102) intensity was increased due to crystallite growth compared to the other coatings. The prominent plane (211) of 117-mHAp was enhanced in comparison with the other modified coatings. It resembles to the plane (211) of pristine.

The microstrain of the modified nanocomposite coatings was varied (Table 1) due to fluctuation in the lattice relaxation and nitrogen bonding. Implantation varies oxygen vacancies to modify the phosphorous-oxygen coordination and concomitant with the lattice parameters and microstrain of the surface modified coatings. The localization of phonon momentum was high in some plane orientations and restricted in certain lattice plane directions leading to decrease the microstrain and altering lattice parameters. This evidently depicts the co-existence of crystalline-partial amorphous of surface modified coatings varied with respect to the ion fluences. At 2517-mHAp, the major lattice plane intensity is reduced (left side of Fig.1) due to a projected lattice vibration and defects. So, the average crystallite size is decreased due to a compressive strain in certain major planes and a relaxed strain in minor planes [46]. Similar type of lattice constant reduction by manganese ions implantation on aluminium thin films [47]. The planes (211) and (221) of 117-mHAp are augmented (left side of Fig.1) when compared to the other implanted samples owing to defects induced plane orientation. Thus, the crystallite size, lattice parameters and microstrain of surface-modified coatings were varied due to the coexistence of partial crystalline-amorphous, defects and disorder.

Table 1 Average crystallite size, lattice parameters and microstrain of the pristine and the ion implanted samples

Samples ID	Average Crystallite size (±1 nm)	Lattice parameters (Å) (±0.01)		Microstrain (±0.001)
		a = b	C	
p-mHAp	56	9.40	6.87	0.009
116-mHAp	14	9.43	6.98	0.030
516-mHAp	20	9.42	6.87	0.003
117-mHAp	29	9.43	6.90	0.008
2517-mHAp	11	9.33	6.88	0.002

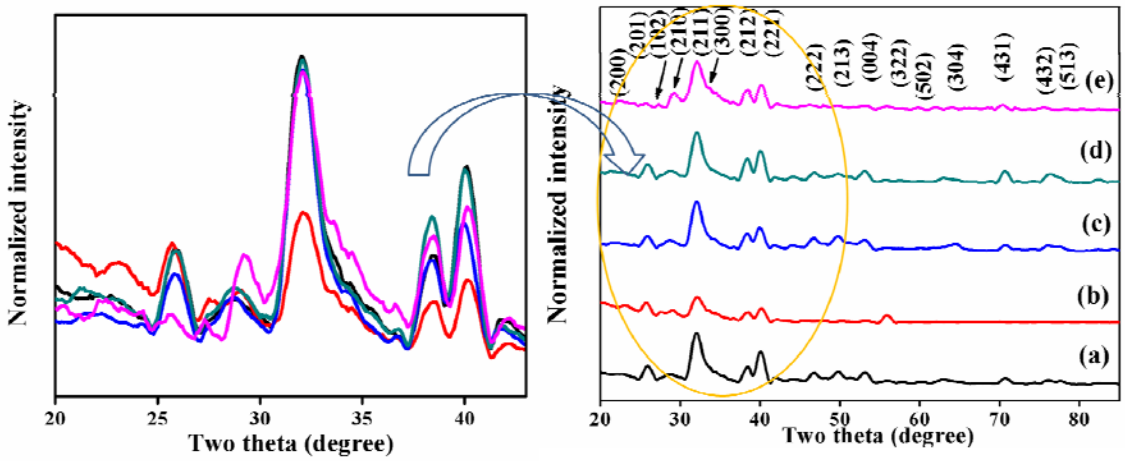

Fig.1. GIXRD patterns of the (a) p-mHAp, (b) 116-mHAp, (c) 516-mHAp (d) 117-mHAp and (e) 2517-mHAp (left side magnified view of Fig.1) and all the peaks in the patterns are corresponding to the phase of HAp particles.

3.2. Raman Analysis

Raman spectra of the coatings are shown in Fig. 2(a) and confocal micro-Raman images of the modified coatings are as shown in Fig. 2(b). Grains split at 116-mHAp and at higher fluences, the splitting was varied due to localized heat fluctuation. The vibrational modes of coatings were altered on implantation. Free PO_4^{3-} tetrahedrons possess four different frequencies ν_1, ν_2, ν_3 and ν_4 [48]. The internal PO_4^{3-} bands are found at ~95 cm^{-1} and 223 cm^{-1} due to the translational motion of calcium and phosphate and whirling of phosphate

group respectively (left side magnified view of Fig.2(a)). The PO_4^{3-} internal bands of 116-mHAp, 117-mHAp and 2517-mHAp are blue shifted compared to pristine due to lattice compressive stress. However, this band is not shifted in 516-mHAp but its intensity enhanced due to a variation in phonon momentum. At 2517-mHAp, the PO_4^{3-} band was augmented due to the formation of strong bond between nitrogen-phosphorus atoms whereas, it was weak in other surface modified coatings.

The symmetric O-P-O (ν_2) (at 421 cm^{-1}) of HAp was varied on implantation. The unfold P-O is found at 962 cm^{-1} which red shifted in 116-mHAp and 117-mHAp due to tensile strain and disordered to N-O-P (inset magnified view of Fig. 2(a)). In 2517-mHAp, the P-O bonding becomes P-N. The triply degenerated mode of asymmetric P-O stretching (1048 cm^{-1}) is noticed only in pristine and disappeared in other implanted samples. The unfold of CH and CH stretching of CH_2 of PVA are noticed at 2721 cm^{-1} and 2914 cm^{-1} respectively. The peak of PVA (2914 cm^{-1}) is only observed in pristine and 516-mHAp compared to other samples and the peak is enhanced in 516-mHAp due to N-C-H-H bond. In other implanted samples, the polymer peak was blue shift due to compressive strain in the polymer chain. Similarly, the CH_2 wagging and the twining mode of OH in the PVA are observed at 1356 cm^{-1} [49]. The peak at 1576 cm^{-1} was intense at pristine, 516-mHAp and 2517-mHAp compared to other samples due to a strong bonding between the polymer and calcium phosphate [50]. This peak intensity was varied drastically owing to the robust influence of defects and vacancies. There are some reports on Raman analysis for the investigation of oxygen vacancy [51-52]. L. Z. Liu et al. reported that oxygen vacancy associated Raman modes of SnO_2 nanocrystals. When the nanocrystals (NCs) were annealed at 1000 °C, the oxygen vacancies were highly reduced which indicated in the Raman spectrum as a shoulder band. Raman spectrum of annealed sample in vacuum was altered the shoulder band hardly [51]. Raman spectra were intense and sharp due to the assembly of interface vacancies and increased vacancy clusters in SnO_2 reported by K. N. Yu et al. [52].

Further, they explained that the Raman intensity augmented with broadened linewidth due to the densities of vacancy clusters and an increase of local SnO_2 cluster. Here, Raman analysis is used to analyze the oxygen vacancies in the coatings. Raman shift and its intensity can be correlated to oxygen vacancies in the coating [51-52]. The intensity of symmetric O-P-O (ν_2) of HAp (at 421 cm^{-1}) was drastically decreased and red shifted in 117-mHAp in comparison with all other coatings that revealing higher oxygen vacancies in the coating. In 116-mHAp and 117-mHAp, the unfold P-O peak (at 962 cm^{-1}) was red shifted which indicating higher oxygen vacancies than other coatings, whereas it was enhanced at 2517-mHAp leads to the reduction of oxygen vacancies due to the presence of higher content of nitrogen ions. The shoulder peak at 1356 cm^{-1} (OH mode) and prominent peak at 1576 cm^{-1} in 117-mHAp was completely red shifted and their intensity also reduced which displaying higher oxygen vacancies in polymer matrix than other coatings. However, in 2517-mHAp, the shoulder peak and prominent peak again enhanced and almost similar to pristine demonstrating that the oxygen vacancies were decreased due to the occurrence of abundant nitrogen ions in the coating. In 117-mHAp, the higher oxygen vacancies and disorder are noticed in comparison with other coatings.

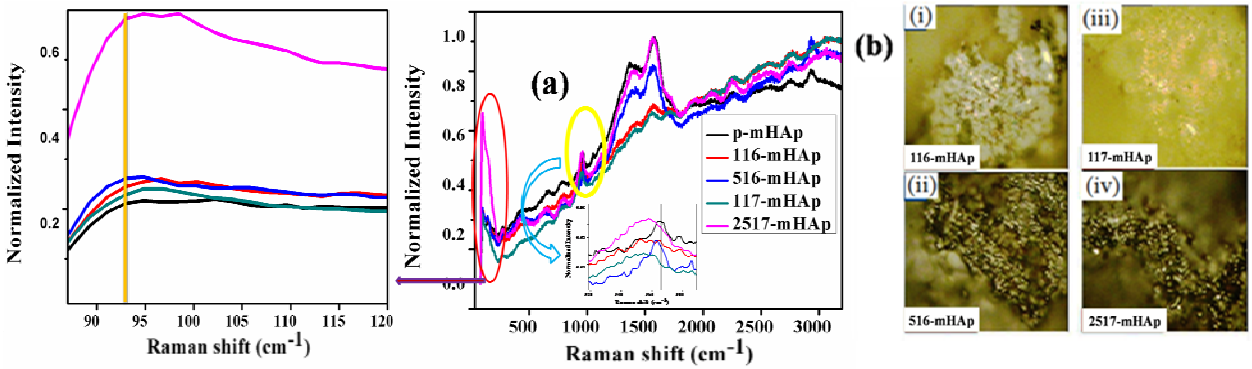

Fig.2. (a) Raman spectra of the pristine and the ion implanted samples (left size magnified view in the range 87 to 120 cm^{-1} of **Fig.2.**(a))(inset magnified view of **Fig.2**.(a)) and (b) Confocal Micro-Raman images of the ion implanted samples.

3.3. Electrical measurement

Electrical resistances of the coatings are as shown in Fig.3a and it was non-linear with the ion fluences. On implantation, the electrical resistance was enhanced up to 117-mHAp and in 2517-mHAp, it was decreased (77 %) compared to pristine. The electrical resistance is maximum at 117-mHAp due to augmented electron scattering in the polymer chains, higher oxygen vacancies, nitrogen bonding with carbon, and phosphorous. Further, the electrons were transferred to nitrogen atoms and creating a strong bonding with the P-O and restricts delocalization of charge carriers due to the high electronegativity of nitrogen atoms. Moreover, the electronic density of nitrogen atoms is enhanced and pushing the Fermi level of other nearby atoms towards vacancy band. Thus, free charge carrier dynamics are limited at 117-mHAp. At 2517-mHAp, the trapped charge carriers are delocalized to increase the conductive paths [53]. The pristine possesses a low resistance and on implantation, the resistance was enhanced due to the co-existence of crystalline-partial amorphous leading to a localization of charge carriers. So, up to the 117-mHAp, the electrical resistance was enhanced due to higher oxygen vacancies, local atomic hybridization, and scattering effect. In 2517-mHAp, the reduced oxygen vacancies and high disorder lead to a decrease in the electrical resistance by the creation of nanochannel paths for conduction, in turn improving the calcification and bone mineralization [54]. The electrical resistance of the coating is a crucial parameter to corrosion resistance under aggressive environment. The implantation passivates the surface and subsurface but not modify the bulk which enables to withstand in atmosphere, electrochemical and biochemical reactions.

3.4. Mechanical strength

On implantation, the microhardness of coating is enhanced and at 2517-mHAp, it was reduced (Fig.3b). In 117-mHAp, the microhardness was 4% enhanced in comparison with pristine due to higher tensile strain and bond strength. Further, the high bond strength and disorder impact to create the strong grain boundaries reduce the sliding displacement of

grains and carbon chains in 117-mHAp. At 2517-mHAp, the microhardness was decreased by 1.5%, due to a greater radiation damage on the grain boundaries and strain relaxation leading to deformation of the coatings. Stable microhardness was attained up to ion fluence 5×10^{16} ions/cm^2 compared to pristine and a similar mechanical behavior explained by Ma et al. [55]. Multiwalled carbon nanotubes (MWCNT) with HAp-chitosan composite coating was deposited on titanium which augmented adhesive strength, microhardness, corrosion resistance and apatite growth reported by Rath et al. [56]. Here, as the ion fluence increases, the microhardness was enhanced due to the grain boundary strength and the optimized crystallinity leads to transfer the applied mechanical energy. Further, the high electronegativity of nitrogen atoms attracts many electrons from surrounding atoms, thus the interatomic distance varied to form strong bonding in the coatings. At 117-mHAp, many electrons were trapped at oxygen vacancy sites responsible to transfer the mechanical energy from nano to micro further to macro-level. This transfer is very weak in 2517-mHAp. The above mentioned mechanisms occur on the surface and subsurface up to 302 nm. The variation of co-existence of crystalline-partial amorphous, bond strength, disorder and grain boundary strength were responsible for different mechanical potency of the surface modified coatings. The adhesiveness of coating to the titanium substrate can be qualitatively accessed by a scotch tape route. The optical images of p-mHAp are shown in Fig.4(a) (before peel test) and Fig.4(b) (after peel test). The peel test reveals no delamination of the coating and the glue from scotch tape is adhered on the coating surface (Fig.4(b)) due to the strong adhesive strength of coating.

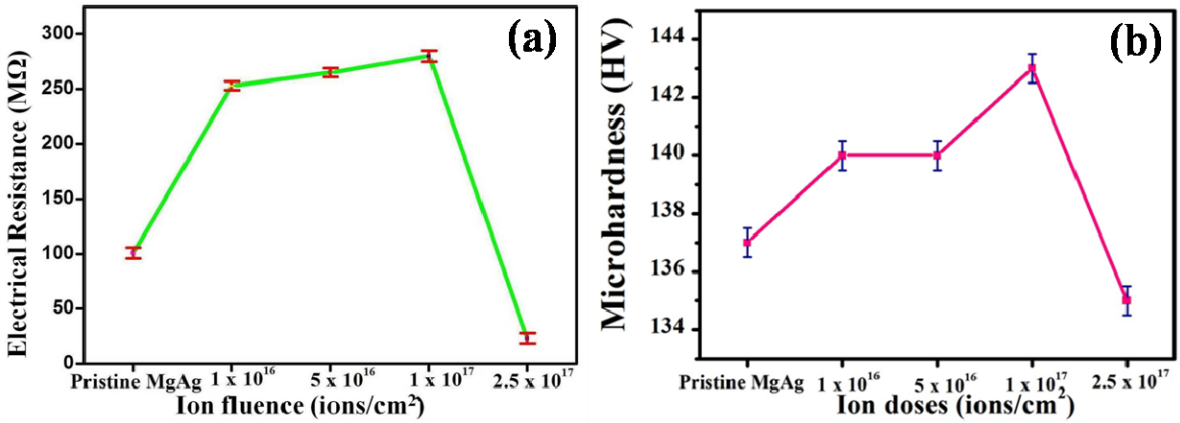

Fig.3 (a) Electrical resistance versus ion fluences and (b) Microhardness of the pristine and the ion implanted samples.

3.5. SEM Analysis

SEM micrograph of p-mHAp was as shown in Fig.4(c) and small pore sizes (~0.25 µm) observed on the coating. The thickness of coating (p-mHAp) was around 175 µm (Fig.4(d)) and the projected range of N^+ ions was 302 nm and hence it did not modify the bulk properties of coatings. The EDX spectrum of p-mHAp is shown in Fig.4(e) and displays the occurrence of calcium, phosphorus and their calcium/phosphorus ratio (1.72) and further the incorporated $Mg^{2+}$and Ag^{1+} and O^{2-} also confirmed (Table 2).

Table 2 EDX of the p-mHAp.

Samples ID	**Calcium (± 0.1%)**	**Phosphorus (± 0.2%)**	**Magnesium (± 0.1%)**	**Silver (±0.1%)**	**Oxygen (± 0.2%)**
p-mHAp	23.35	13.57	0.82	1.76	41

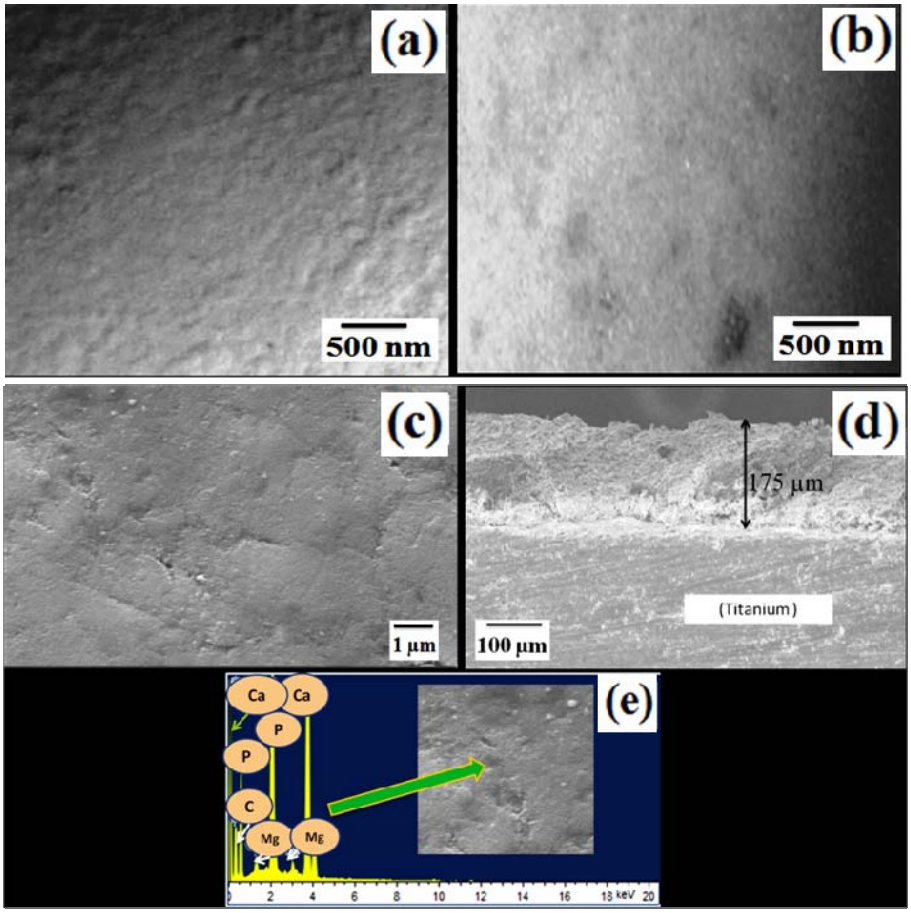

Fig.4. Optical images of the p-mHAp (Pristine) (a) before peel test and (b) after peel test; (c) SEM micrograph of the p-mHAp; (d) SEM of the thickness of the pristine (p-mHAp) and (e) EDX spectrum of the p-mHAp.

3.6. AFM Analysis

The 2D (Dimensional) surface topography of coatings is as shown in Fig.5. The average surface roughness and pore size are enhanced on ion implantation. At higher fluence (2517-mHAp), they are reduced (Table 3). The surface roughness is found to enhance (4.5 times) in 516-mHAp due to the ion sputtering and grooving effect, leading to the formation of deep grooves between the larger particles (Fig.5). In 116-mHAp, these effects were weak however, the average pore size was superior in comparison with the other coatings. As the fluence increases, the surface roughnesses are reduced drastically due to localized heating leads to melt the surface of coating. Here, the ion-induced diffusion and localized heating

were varied on ion fluences which split the agglomerated particles to smaller size leading to reduce the surface roughness (2517-mHAp) [57]. The surface properties play a vital role for leaching effect due to high interaction of particles with liquid. Thus, the low energy surface modification tailors the leaching or degradability of the coatings.

Table 3 Average roughness and average pore size of the (a) p-mHAp, (b) 116-mHAp, (c) 516-mHAp, (d) 117-mHAp and (e) 2517-mHAp.

Samples ID	Average roughness (± 1 nm)	Average pore size (± 0.1 µm)
p-mHAp	146.0	2.90
116-mHAp	350.9	7.01
516-mHAp	664.8	3.67
117-mHAp	167.7	3.50
2517-mHAp	135.6	3.30

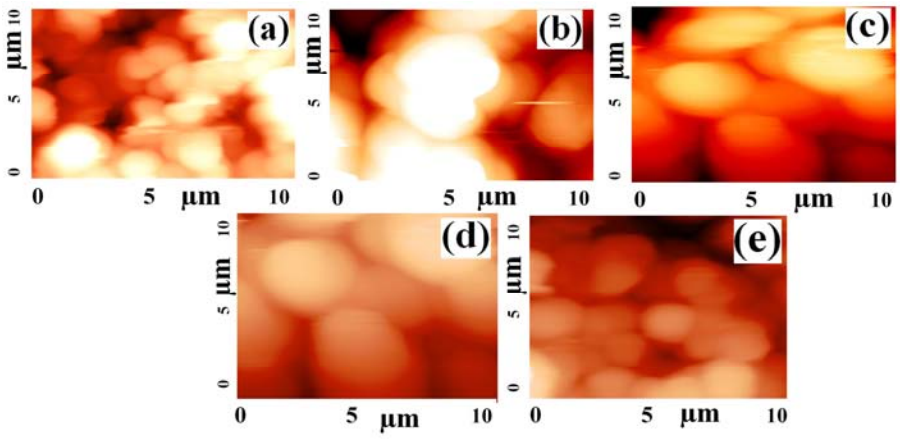

Fig.5. AFM of the (a) p-mHAp, (b) 116-mHAp, (c) 516-mHAp, (d) 117-mHAp and (e) 2517-mHAp.

3.7. Wettability

Wettability of the pristine and surface modified coatings is as shown in Fig.6. The water contact angles of pristine, 116-mHAp, 516-mHAp, 117-mHAp and 2517-mHAp are found 3±1°, 37±1°, 73±1°, 40±1° and 36±1° respectively. The wettability of implanted samples was

reduced in comparison with pristine. The contact angles of coatings were varied due to ion induced chemical changes in bonding, surface roughness, and surface charges. The surface of pristine is superhydrophilic whereas, it changed to hydrophobic in 516-mHAp due to the highest surface roughness which is consistent with the results of Zhao et al. [58]. In other implanted samples, the wettability was enhanced due to a decrease in the surface roughness. The crystallinity, oxygen vacancies and disorder of surface modified coatings are associated for the modulation of surface roughness thereby, the wettability was altered. In pristine, the crystalline-partial amorphous phase was not noticed and its surface possesses hydroxyl, phosphate and CH_2/CH group of polymer. When water molecules interact with these groups to form hydrogen bonding leads to superhydrophilic surface. Moreover, these groups were favorable to polarize charges to create bonding with water molecules. In 516-mHAp, the surface projected atomic groups facilitate to a very high contact angle. Further, the water molecules were highly repelled on its surface owing to different orientations of charge polarization leading to a weak hydrogen bonding. At 2517-mHAp, there was a slight increase in the wettability due to the variation in the charge polarization by the impact of N^+ ions bonding. The N^+ ions are electronegative leading to change the charge polarization direction by attracting many electrons. The other reason for weak hydrophilic surface was due to trapped electrons. So, the oxygen vacancies, disorder and bonding were highly responsible to modify the contact angles of modified coatings compared to pristine. Thus, the implantation opens a path to tailor superhydrophilic surface to weak hydrophilic without using hydrophobic colloidal molecules. Further, it reduces the processing time to develop hydrophobic surface for controlling corrosion rate [59]. The p-mHAp assists DNA adsorption owing to the occurrence of phosphate in DNA. The interactions of cell with material were varied on different surface properties reported by Das et al [60]. The adhesions of coating and surface chemistry were also altered by ion implantation [61]. The ion implanted coatings

possess a weak hydrophilic surface to support anticorrosion and absorption of protein (Bovine serum albumin).

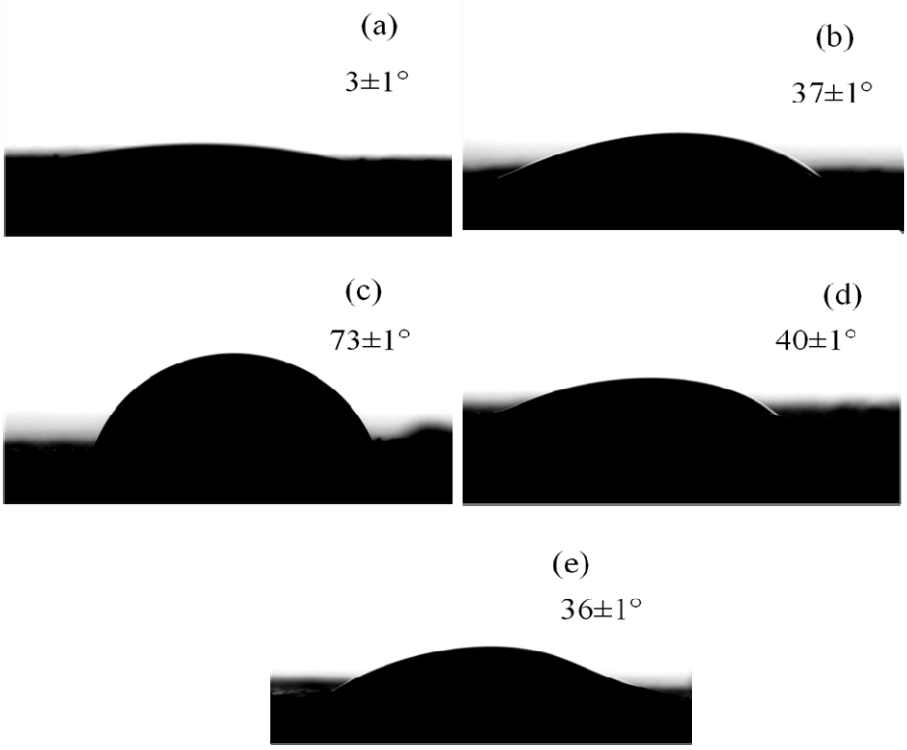

Fig.6. Wettability of the (a) p-mHAp, (b) 116-mHAp, (c) 516-mHAp, (d) 117-mHAp and (e) 2517-mHAp.

3.8 Immersion test

The corrosion property of the coatings is evaluated by immersion test in Phosphate buffer solution (PBS) for 24 hours and 96 hours. Weight of the coatings (W_0) is measured before immersion test. After immersion test for 24 hours and 72 hours in PBS then, all the coatings are weighed again (W_1). The weight loss (W) in the coating weight can be correlated to the coating evolution, bond strength and corrosion resistant of coatings. The weight loss can be calculated by the following equation 2 [62],

$$W\ (g/cm^2) = \frac{[W_0 - W_1]}{A} \text{ ---------- (2)}$$

Here, A is the surface area of coating (cm^2). The weight loss of coatings on the immersion test in PBS for different time periods is mentioned in Table 4 and revealed that all the surface modified coatings are stable. Especially, the weight loss in 117-mHAp coating (1×10^{17} ions/cm^2) for 24 hours and 96 hours is less compared to other coatings. This evidently shows that the 117-mHAp possesses less dissolution in comparison with other coatings due to the high bond strength and corrosion resistant.

Table 4 Weight loss of pristine and ion implanted coatings during immersion in PBS for different time periods

Sample	**Weight loss after 24 hours (g/cm^2)**	**Weight loss after 96 hours (g/cm^2)**
Pristine	0.035 (±0.003)	0.063 (±0.002)
116-mHAp	0.045 (±0.002)	0.076 (±0.003)
516-mHAp	0.024 (±0.003)	0.044 (±0.003)
117-mHAp	0.011 (±0.002)	0.026 (±0.003)
2517-mHAp	0.061 (±0.003)	0.096 (±0.002)

3.9. Corrosion studies

The potentiodynamic anodic polarization of the coating is as shown in Fig.7. The corrosion related parameters corrosion potentials (E_{corr}) and corrosion current density (I_{corr}) were quantitatively measured from the polarization plots (Table 5). On implantation, the corrosion potential of coatings was enhanced towards positive side of potential thereby, I_{corr} was reduced due to a high corrosion resistance. Both the cathodic and anodic reactions were shifted the polarization curve towards a low current density on implantation leads to the reduction of the degradation rate. In 117-mHAp, the corrosion resistance was enhanced due

to a higher corrosion potential (84.6 %, -0.02 V) with a significant decrease in the I_{corr} (7.91×10^{-8} Acm^{-2}) compared to other coatings which also confirmed from electrical resistance measured before corrosion studies. When the surface of 117-mHAp interacts with the hank's solution possesses a weak surface oxidation and leaching owing to the strong bonding of N^{+} ions in the coatings. In 2517-mHAp, the corrosion resistance was reduced in comparison with p-mHAp due to the decreased corrosion potential (46%) and surface resistance lead to a high metal ion dissolution from the coating surface. Further, the generation of nanochannels and conductive paths were high in 2517-mHAp responsible for high corrosion on the coating. In 116-mHAp, the corrosion resistance is reduced due to a rough surface exposed to hank's solution leading to a greater release of metal ions by oxide degradation or micro-level corrosions [63]. However, the 516-mHAp has the highest surface roughness compared to the other samples but it shows a good corrosion resistance in comparison with 116-mHAp. Therefore, apart from the surface roughness, the other parameters such as bond strength, and disorder are also play a crucial role for the enhancement of corrosion resistance. Here, the optimized crystallinity, disorder, bond strength, surface roughness and surface resistance are responsible for a very high corrosion resistance in 117-mHAp compared to other coatings. Hence, the implantation tailors the aforementioned parameters for better anticorrosion coatings at the *in vitro* level.

Table 5 Corrosion parameters for the p-mHAp and the ion implanted samples

Samples ID	**Corrosion potential (E_{corr}) (V)**	**Corrosion current density (I_{corr}) (Acm^{-2})**
p-mHAp	-0.13	$2.75\ x10^{-7}$
116-mHAp	-0.17	$3.88\ x10^{-7}$
516-mHAp	-0.07	$5.52\ x10^{-8}$

117-mHAp	-0.02	7.91×10^{-8}
2517-mHAp	-0.19	6.11×10^{-7}

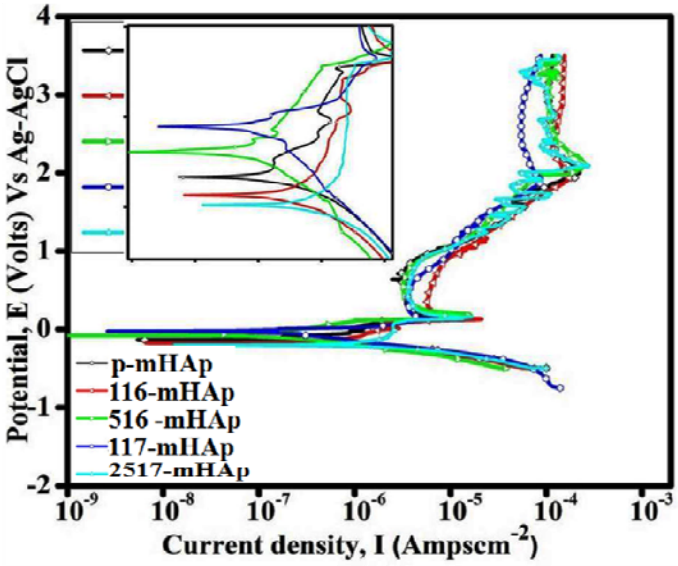

Fig.7. Potentiodynamic polarization plots of the pristine and the ion implanted samples.

The Nyquist plots of coatings are as shown in Fig.8(a) and show an incomplete semicircular arc. As the real part of impedance increases, the imaginary part elevates linearly indicating a stable anticorrosion coating on implantation. At 117-mHAp, the capacitive loop was augmented because of high resistance leads to the reduction of corrosion rate in comparison with other coatings. The coating resistance of 2517-mHAp was reduced confirmed from Fig.8(a) and also corroborated from Fig.3a due to high disorder and weak bond strength. The optimized crystallinity, disorder and bond strength are favorable for a high coating resistance in 117-mHAp for superior corrosion resistance. Generally, the materials show high resistance with low capacitance offers a better corrosion resistance and vice versa.

The Bode plots of coatings provide an insight into the corrosion mechanism and impedance (Fig.8(b)). On implantation, the impedance of coating is enhanced at low frequency. In 117-mHAp, the high impedance is achieved which well-matched with the

Nyquist plot due to optimized disorder and surface roughness. The impedance of 2517-mHAp is reduced owing to a high radiation damage compared to other coatings. The phase angle of surface modified coatings was augmented in comparison with pristine. In 117-mHAp, the phase angle was maximum (-80º) compared to the other coatings (Fig.8(c)) illustrating a passive surface with a capacitive behaviour from low to medium frequency. Further, a constant phase is confirmed in 117-mHAp at high impedance. At 2517-mHAp, the phase angle was least (-10°) compared to the phase angles of other coatings indicating less impedance. In other coatings, the phase angles also modified due to the fluctuation of coating resistance by ion-induced defects and disorder.

The equivalent circuit model was employed to fit EIS of the specimen (Fig.8(a)(inset)). The EIS parameters are obtained after the fittings and mentioned in Table 6. The EIS spectra of coatings are suited to the model ($R_s(R_{oc}Q_{oc})(R_{is}Q_{is})$)[Fig.8(a)(inset)], the R_s denotes solution resistance, the R_{oc} and R_{is} denote the resistance of outer coating surface and inner substrate respectively. Where, Q_{oc} and Q_{is} are the double-layer capacitance of the outer coating surface and the inner substrate respectively. All the specimens show two-layer model due to the inner substrate and the external coating layers. In titanium alloy, the two time constants on its surface were reported by Tamilselvi and Rajendran [64]. Constant Phase Element (CPE) is suggested for fitting and matched well between the simulated and experimental data. The CPE impedance is defined by equation 3 [64].

$$Z_{CPE} = \left[Q(j\omega)^n\right]^{-1} \text{---------- (3)}$$

Where, Q, ω and n are the level of CPE, angular frequency and exponent of the CPE respectively and its values in the range -1 and 1 are associated to irregular current due to roughness, disorder and bond strength.

The frequency independent parameter, n_{oc} is near to 1 in all the specimens (Table 6) except at 116-mHAp, indicating near capacitive behavior of the coating due to the porous surface.

Moreover, its outer coating resistance was slightly comparable with respect to the other modified samples and showed an ideal capacitor behavior. The coating resistance of 117-mHAp was greater compared to other coatings due to the optimized disorder, bond strength, localized charge carrier and R_{oc} which demonstrating an excellent anticorrosion behavior.

Table 6 EIS parameters of the p-mHAp and the ion implanted samples

Samples ID	$\mathbf{R_s}$ kΩ cm^2	$\mathbf{Q_{oc}\times10^{-8}}$ Fcm^{-2}S^n	$\mathbf{R_{oc}}$ kΩcm^2	n_{oc}	$\mathbf{Q_{is}\times10^{-5}}$ Fcm^{-2}S^n	$\mathbf{R_{is}}$ kΩ cm^2	$\mathbf{n_{is}}$
p-mHAp	44.84	2.891	4.05	0.99	5.036	187061	0.82
116-mHAp	350.2	4.745	48.0	0.21	5.465	138950	0.81
516-mHAp	419.0	5.536	94.23	0.98	5.300	127220	0.82
117-mHAp	399.1	4.713	190.3	0.94	4.154	177336	0.88
2517-mHAp	374.8	3.033	39.76	0.95	4.048	111560	0.81

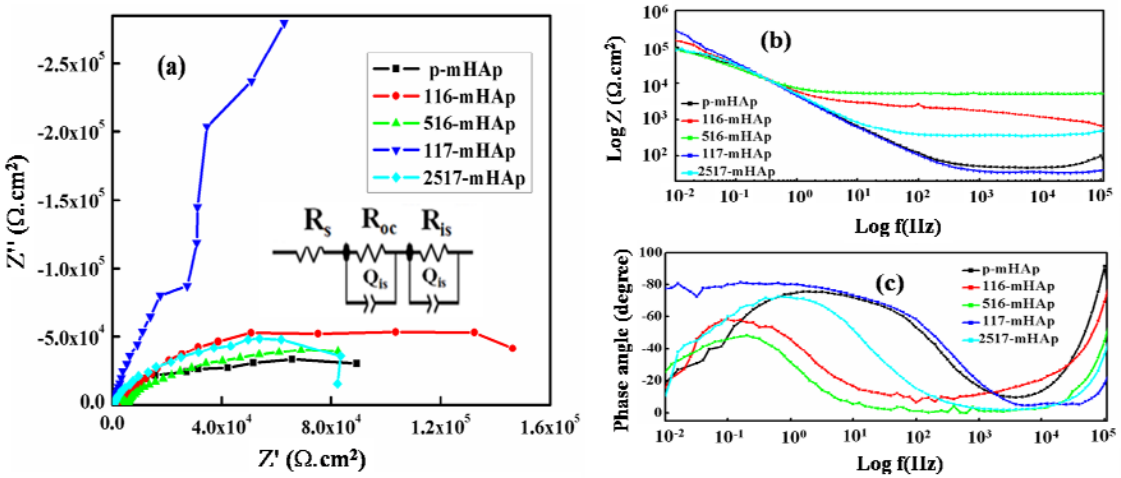

Fig.8. (a) Nyquist plots of the pristine and the ion implanted samples (inset figure Equivalent circuit model used for the impedance analysis), (b) Bode impedance plots of the pristine and the ion implanted samples and (c) Bode phase angle plots of the pristine and the ion implanted samples.

High corrosion potential and less weight loss are noticed in 117-mHAp compared to other coatings. It is due to the optimized crystallinity, disorder, bond strength of N-O-P (962 cm^{-1})

and surface roughness leading to the reduction of coating degradation rate. These parameters are responsible for the surface passivation of coating. In 2517-mHAp, the corrosion potential is low and high weight loss attained due to radiation damage in coating and higher content of nitrogen ions leads to the reduction of bond strength of N-O-P. Thus, the crystallinity, disorder, bond strength and surface roughness are favorable parameters for the enhancement of anticorrosion in coating.

4. Conclusions

The 70 keV N^+ ions were implanted on the polymer-based Mg-Ag ions co-incorporated HAp nanocomposite coating by microwave-assisted deposition. As ion fluences increase, the crystallinity of coatings was varied which confirmed by GIXRD patterns. The crystallite size of 2517-mHAp was significantly reduced by 80%. The compressive and tensile strains of modified coatings were confirmed by Raman analysis. The electrical resistance of 117-mHAp was enhanced (2.7 times) compared to pristine whereas, in 2517-mHAp, it was decreased. The mechanical strength of 117-mHAp is elevated in comparison with other coatings. The surface roughness, pore size and contact angle of coatings are augmented on ion implantation. The corrosion potential was enhanced in 117-mHAp due to the high impedance confirmed by Nyquist plot and Bode plot. The crystallinity, bond strength, surface roughness and wettability are engineered on implantation which are responsible factors for the enhancement of anticorrosion in 117-mHAp. The bond strength and surface roughness play a dominant role for high corrosion resistant leads to passivate the surface of modified coatings. Here, the dissolution of coating is reduced by the formation of N-O-P bond which is strong in 117-mHAp compared to other coatings. These basic and applied understandings pave a path to develop advanced anticorrosion coatings.

Acknowledgements

Author (K.T.A) grateful to Materials Science Group, IGCAR, Kalpakkam, Tamil Nadu, India for granting permission to perform ion implantation.

References

[1] M. Pourbaix, Electrochemical corrosion of metallic biomaterials, Biomaterials. 5 (1984) 122-134.

[2] F.W.S. Jr, Carcinogenicity of metal alloys in orthopedic prostheses: clinical and experimental studies, Fundam. Appl. Toxicol. 13 (1989) 205-216.

[3] W.N. Capello, J.A. D'Antonio, R.G. Geesink, J.R. Feinberg, M. Naughton, Late remodeling around a proximally HA-coated tapered titanium femoral component, Clin. Orthop. Relat. R. 467 (2009) 155-165.

[4] R. Comesaña, F. Lusquinos, V.J. Del, F. Quintero, A. Riveiro, M. Boutinguiza et al., Toward Smart Implant Synthesis: Bonding Bioceramics of Different Resorbability to Match Bone Growth Rates, Sci. Rep. 5 (2015) 10677

[5] S.I. Roohani-Esfahani, P. Newman, H. Zreiqat, Design and Fabrication of 3D printed Scaffolds with a Mechanical Strength Comparable to Cortical Bone to Repair Large Bone Defects, Sci. Rep. 6 (2016) 19468.

[6] D.M. Liu, Q. Yang, T. Troczynski, Sol–gel hydroxyapatite coatings on stainless steel substrates, Biomaterials. 23 (2002) 691-698.

[7] C.K. Wang, J.H.C. Lin, C.P. Ju, H.C. Ong, R.P.H. Chang, Structural characterization of pulsed laser-deposited hydroxyapatite film on titanium substrate, Biomaterials. 18 (1997) 1331-1338.

[8] A. Stoch, A. Brozek, G. Kmita, J. Stoch, W. Jastrzębski, A. Rakowska, Electrophoretic coating of hydroxyapatite on titanium implants. J. Mol. Struct. 596 (2001) 191-200.

[9] F. Liu, J. Xu, F. Wang, L. Zhao, T. Shimizu, Biomimetic deposition of apatite coatings on micro-arc oxidation treated biomedical NiTi alloy, Surf. Coat. Technol. 204 (2010) 3294-3299.

[10] A.E. Porter, L.W. Hobbs, V.B. Rosen, M. Spector, The ultrastructure of the plasma-sprayed hydroxyapatite–bone interface predisposing to bone bonding, Biomaterials. 23 (2002) 725-733.

[11] Y.P. Lu, M.S. Li, S.T. Li, Z.G. Wang, R.F. Zhu, Plasma-sprayed hydroxyapatite-+titania composite bond coat for hydroxyapatite coating on titanium substrate, Biomaterials. 25 (2004) 4393-4403.

[12] M. Manso, C. Jimenez, C. Morant, P. Herrero, J.M. Martínez-Duart, Electrodeposition of hydroxyapatite coatings in basic conditions, Biomaterials. 21 (2000) 1755-1761.

[13] Y.Y. Zhang, J.Tao, Y. Pang, W. Wang, T. Wang, Electrochemical deposition of hydroxyapatite coatings on titanium, Trans. Nonferrous Met. Soc. China. 16 (2006) 633-637.

[14] X. Zhao, L. Yang, Y. Zuo, J. Xiong, Hydroxyapatite Coatings on Titanium Prepared by Electrodeposition in a Modified Simulated Body Fluid. Chin. J. Chem. Eng. 17 (2009) 667-671.

[15] S.A.R. Ananda, C. Lautaret, S. Gorelick, M. Laitinen, P. Rahkila, M. Putkonen, et al. Ion-sputtering deposition of Ca–P–O films for microscopic imaging of osteoblast cells, Nucl. Instrum. Methods Phys. Res. 261 (2007) 719-722.

[16] D. Tadic, M. Epple, Mechanically stable implants of synthetic bone mineral by cold isostatic pressing, Biomaterials. 24 (2003) 4565-4571.

[17] F.A. Espana, V.K. Balla, S. Bose, A. Bandyopadhyay, Design and fabrication of CoCrMo alloy based novel structures for load bearing implants using laser engineered net shaping, Mater. Sci. Eng. C. 30 (2010) 50-57.

[18] M. Hamdi, A.M. Ektessabi, Electron beam deposition of thin bioceramic film for biomedical implants, Thin Solid Films. 398-399 (2001) 385-390.

[19] H.H. Rodríguez, G. Vargas, D.A. Cortes, Electrophoretic deposition of bioactive wollastonite and porcelain–wollastonite coatings on 316L stainless steel, Ceram. Int. 34 (2008) 1303-1307.

[20] M. Javidi, S. Javadpour, M.E. Bahrololoom, J. Ma, Electrophoretic deposition of natural hydroxyapatite on medical grade 316L stainless steel, Mater. Sci. Eng. C. 28 (2008) 1509-1515.

[21] Z. Wang, P. Xiao, J. Shemilt, Fabrication of composite coatings using a combination of electrochemical methods and reaction bonding process, J. Eur. Ceram. Soc. 20 (2000) 1469-1473.

[22] J. Lamaming, N. B. Heng, A.A. Owodunni, S.Z. Lamaming et al. Characterization of rubberwood particleboard made using carboxymethyl starch mixed with polyvinyl alcohol as adhesive, Compos. B. Eng. 183 (2020) 107731.

[23] D. Zhitomirsky, J.A. Roether, A. R. Boccaccini, I. Zhitomirsky, Electrophoretic deposition of bioactive glass/polymer composite coatings with and without HA nanoparticle inclusions for biomedical applications, J. Mater. Process. Technol. 209 (2009) 1853-1860.

[24] L. Besra, M. Liu, A review on fundamentals and applications of electrophoretic deposition (EPD), Prog. Mater. Sci. 52 (2007) 1-61.

[25] L. Yang, S. Perez-Amodio, G.F.Y.F. B. de, V. Everts, B.C.A. Van, P. Habibovic, The effects of inorganic additives to calcium phosphate on in vitro behavior of osteoblasts and osteoclasts, Biomaterials. 31 (2010) 2976-2989.

[26] J.D. Featherstone, Prevention and reversal of dental caries: role of low level fluoride, Community Dent. Oral Epidemiol. 27 (1999) 31-40.

[27] J. Althoff, P. Quint, E.R. Krefting, H.J. Hohling, Morphological studies on the epiphyseal growth plate combined with biochemical and X-ray microprobe analyses, Histochemistry. 74 (1982) 541-552.

[28] I.S. Yahia, M. Shkira, S.M.A.S. Keshk, Physicochemical properties of a nanocomposite (graphene oxidehydroxyapatite-cellulose) immobilized by Ag nanoparticles for biomedical applications. Results Phys. 16 (2020) 102990.

[29] H. Cimenoglu, M. Gunyuz, G.T. Kose, M. Baydogan, F. Uğurlu, C. Sener, Micro-arc oxidation of Ti6Al4V and Ti6Al7Nb alloys for biomedical applications. Mater. Charact. 62 (2011) 304-311

[30] M.K. Lei, Y.X. Ou, K.S. Wang, L. Chen, Wear and corrosion properties of plasma-based low-energy nitrogen ion implanted titanium, Surf. Coat. Technol. 205 (2011) 4602-4607.

[31] A.Riveiro, R.Soto, J.D. Val, R. Comesana, M. Boutinguiza, F.Quintero. F.Lusquiños, J. Pou, Laser surface modification of ultra-high-molecular-weight polyethylene (UHMWPE) for biomedical applications, Appl. Surf. Sci. 302 (2014) 236-242.

[32] L. Pramatarova, E. Pecheva, T. Petrov, A. Kondyurin, R. Pramatarova, N. Minkovski, Ion beam and laser processing for hydroxyapatite formation, Vacuum. 76 (2004) 339-342.

[33] Q. Wang, P.Z. Zhang, D.B. Wei, R.N. Wang, X.H. Chen, H.Y. Wang, Microstructure and corrosion resistance of pure titanium surface modified by double-glow plasma surface alloying, Mater. Des. 49 (2013) 1042-1047.

[34] P. Vlcak, Evidence of a defect structure in high fluence nitrogen ion implanted titanium and its effect on corrosion. Results Phys. 11 (2018) 274-277.

[35] P.R. Klokkevold, R.D. Nishimura, M. Adachi, A. Caputo, Osseointegration enhanced by chemical etching of the titanium surface. A torque removal study in the rabbit, Clin. Oral Implants Res.8 (1997) 442-447.

[36] T.B. Ren, T. Weigel, T. Groth, A. Lendlein, Microwave plasma surface modification of silicone elastomer with allylamine for improvement of biocompatibility, J Biomed Mater Res A.86 (2008) 209-219.

[37] D. Aronov, G. Rosenman, Trap state spectroscopy studies and wettability modification of hydroxyapatite nanobioceramics, J. Appl. Phys. 101 (2007) 034701.

[38]F. A. Smidt, Recent advances in the application of ion implantation to corrosion and wear protection, Nucl. Instrum. Methods Phys. Res. 10-11 (1985) 532-538.

[39] M.F. Stroosnijder, Ion implantation for high temperature corrosion protection, Surf. Coat.Technol. 100-101 (1998) 196-201.

[40] H. Pelletier, V. Nelea, P. Mille, D. Muller, Mechanical properties of pulsed laser-deposited hydroxyapatite thin film implanted at high energy with N^+ and Ar^+ ions. Part I: nanoindentation with spherical tipped indenter, Nucl. Instrum. Methods Phys. Res. 216 (2004) 269-274.

[41] M. Yoshinari, Y. Ohtsuka, T. Dérand, Thin hydroxyapatite coating produced by the ion beam dynamic mixing method, Biomaterials. 15 (1994) 529-535.

[42]S.A.R. Ananda, P. Rahkila, M. Vaisanen, R. Lehto, T. Sajavaara, S. Gorelick et al., Wettability and compositional analysis of hydroxyapatite films modified by low and high energy ion irradiation, Nucl. Instrum. Methods Phys. Res. 266 (2008) 2515-2519.

[43] P. Sioshansi, E.J. Tobin, Surface treatment of biomaterials by ion beam processes, Surf. Coat. Technol. 83 (1996) 175-182.

[44]G.S. Chang, J.H. Son, S.H. Kim, K.H. Chae, C.N. Whang, E. Menthe et al., Electronic structures and nitride formation on ion-implanted AISI 304L austenitic stainless steel, Surf. Coat.Technol. 112 (1999) 291-294.

[45] A. Oyane, H.M. Kim, T. Furuya, T. Kokubo, T. Miyazaki, T. Nakamura, J. Biomed. Mater. Res. Part A 65 (2003) 188-195.

[46] C.A. Majid, X-ray investigation of amorphization of ion-implanted Al–Mn, Nucl. Instrum. Methods Phys. Res. 149 (1999) 433-444.

[47]C.A. Majid, Strain-induced amorphization of aluminium by manganese implantation, Philos. Mag. 61 (1990) 769-783.

[48]R. Cusco, F. Guitian, S. D. Aza, L. Artus, Differentiation between hydroxyapatite and β-tricalcium phosphate by means of μ-Raman spectroscopy, J. Eur. Ceram. Soc. 18 (1998) 1301-1305.

[49] Y. Badr, M.A. Mahmoud, Enhancement of the optical properties of poly vinyl alcohol by doping with silver nanoparticles, J. Appl. Polym. Sci. 99 (2006) 3608-3614.

[50] H.L. Chou, C.M. Wu, F.D. Lin, J. Rick, Interactions between silver nanoparticles and polyvinyl alcohol nanofibers, AIP Adv.4 (2014) 087111.

[51] L. Z. Liu, T. H. Li, X. L. Wu, J. C. Shen, P. K. Chu, Identification of oxygen vacancy types from Raman spectra of SnO2 nanocrystals, J. Raman Spectrosc. 43 (2012).

[52] K. N. Yu, Y. H. Xiong, Y. L. Liu, C. S. Xiong, Microstructural change of nano-SnO2 grain assemblages with the annealing temperature Phys. Rev. B 55 (1997) 2666-2671

[53] K. Yokota, K. Nakamura, T. Kasuya, K. Mukai, M. Ohnishi. Resistivities of titanium nitride films prepared onto silicon by an ion beam assisted deposition method, J. Phys. D Appl. Phys. 37 (2004) 1095-1101.

[54] G. Scott, J.B. King, A prospective, double-blind trial of electrical capacitive coupling in the treatment of non-union of long bones, J.Bone Joint Surg. Am. 76 (1994) 820-826.

[55]X. Ma. J. Li, M. Sun, Structure and micro-mechanical properties of helium-implanted layer on Ti by plasma-based ion implantation, Appl. Surf. Sci. 254 (2008) 6837-6841.

[56] P.C. Rath, B.P. Singh, L. Besra, S. Bhattacharjee, Multiwalled Carbon Nanotubes Reinforced Hydroxyapatite-Chitosan Composite Coating on Ti Metal: Corrosion and Mechanical Properties, J. Am. Ceram. Soc. 95 (2012) 2725-2731.

[57] K.A.R. Grayeli, H. Savaloni, Effect of nitrogen ion implantation on corrosion inhibition of nickel coated 316 stainless steel and correlation with nano-structure, Appl. Surf. Sci. 258 (2012) 9982-9988.

[58] Q. Zhao, Y. Liu, C. Wang, S. Wang, N. Peng, C. Jeynes, Reduction of bacterial adhesion on ion-implanted stainless steel surfaces, Med.Eng. Phys. 30 (2008) 341-349.

[59] P.S. Brown, B. Bhushan, Bioinspired, roughness-induced, water and oil super-philic and super-phobic coatings prepared by adaptable layer-by-layer technique, Sci. Rep. 5 (2015) 14030.

[60] K.Das, S. Bose, A. Bandyopadhyay, Surface modifications and cell–materials interactions with anodized Ti, Acta Biomater. 3 (2007) 573-585.

[61] L.Y. Ostrovskaya, Studies of diamond and diamond-like film surfaces using XAES, AFM and wetting, Vacuum. 68 (2002) 219-238.

[62] T.S.N.S. Narayanan Phosphate Conversion Coatings - A Metal Pretreatment Process, Corros. Rev. 12 (2011) 201-238.

[63] M. Browne, P.J. Gregson, Effect of mechanical surface pretreatment on metal ion release, Biomaterials. 21 (2000) 385-392.

[64] S. Tamilselvi, N. Rajendran, In vitro corrosion behaviour of Ti-5Al-2Nb-1Ta alloy in Hanks solution, Mater. Corros. 58 (2007) 285-289.

List of figures

Fig.1. GIXRD patterns of the (a) p-mHAp, (b) 116-mHAp, (c) 516-mHAp (d) 117-mHAp and (e) 2517-mHAp (left side magnified view of Fig.1) and all the peaks in the patterns are corresponding to the phase of HAp particles.

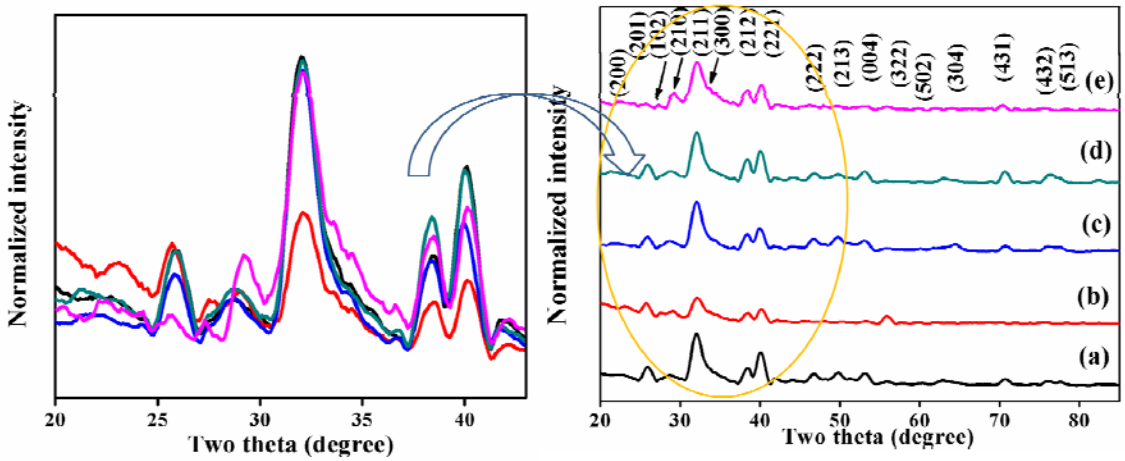

Fig.2. (a) Raman spectra of the pristine and the ion implanted samples (left size magnified view in the range 87 to 120 cm^{-1} of **Fig.2.**(a))(inset magnified view of **Fig.2**.(a)) and (b) Confocal Micro-Raman images of the ion implanted samples.

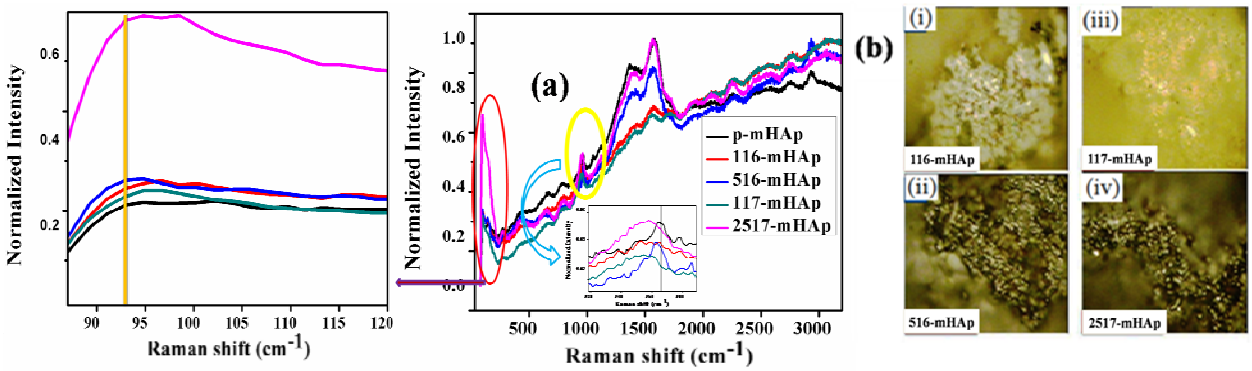

Fig.3 (a) Electrical resistance versus ion fluences and (b) Microhardness of the pristine and the ion implanted samples.

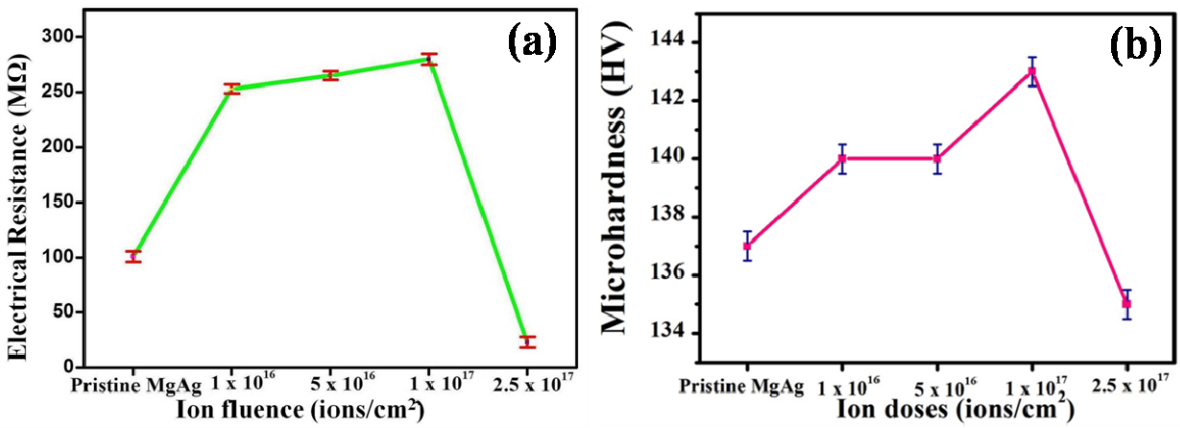

Fig.4. Optical images of the p-mHAp (Pristine) (a) before peel test and (b) after peel test; (c) SEM micrograph of the p-mHAp; (d) SEM of the thickness of the pristine (p-mHAp) and (e) EDX spectrum of the p-mHAp.

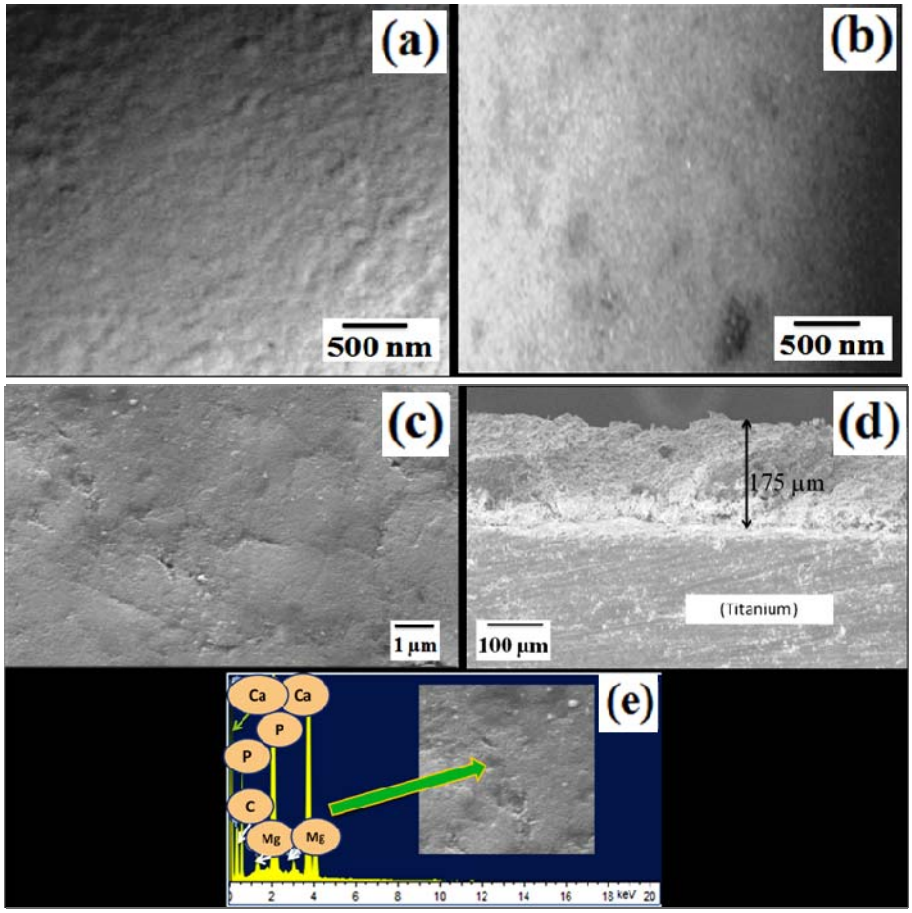

Fig.5. AFM of the (a) p-mHAp, (b) 116-mHAp, (c) 516-mHAp, (d) 117-mHAp and (e) 2517-mHAp.

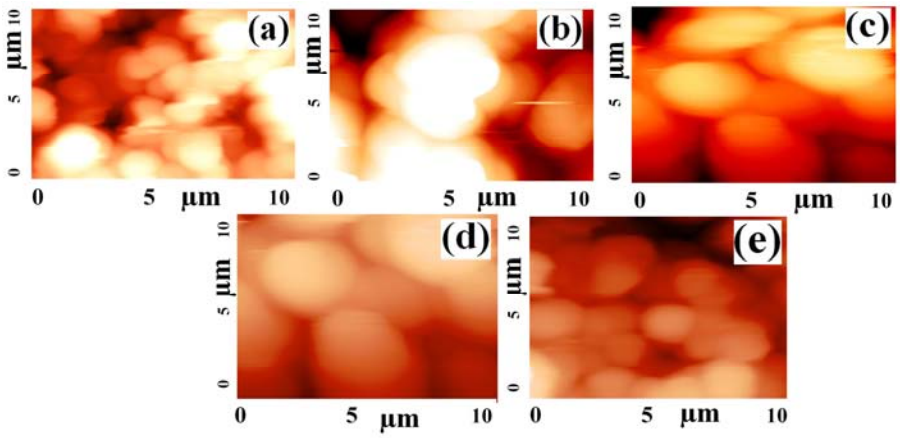

Fig.6. Wettability of the (a) p-mHAp, (b) 116-mHAp, (c) 516-mHAp, (d) 117-mHAp and (e) 2517-mHAp.

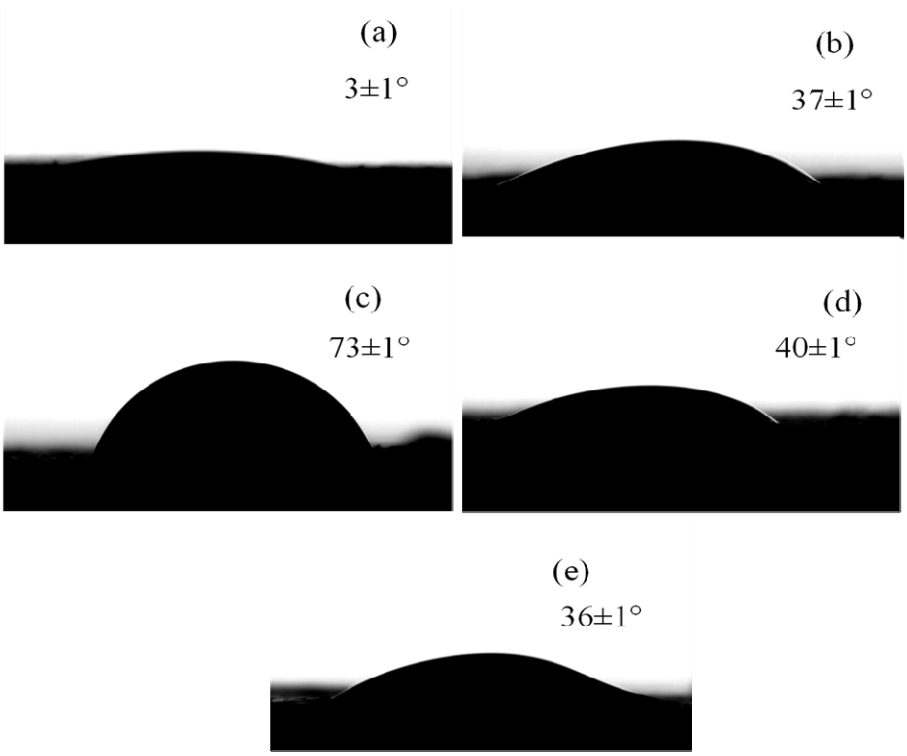

Fig.7. Potentiodynamic polarization plots of the pristine and the ion implanted samples.

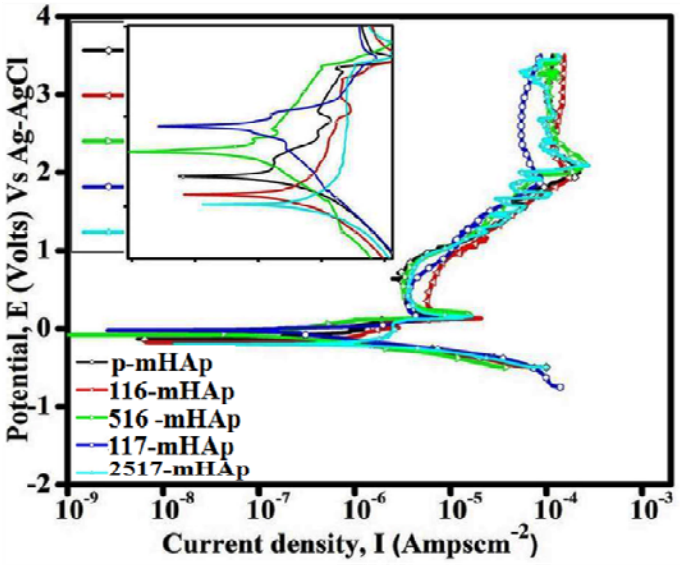

Fig.8. (a) Nyquist plots of the pristine and the ion implanted samples (inset figure Equivalent circuit model used for the impedance analysis), (b) Bode impedance plots of the pristine and

the ion implanted samples and (c) Bode phase angle plots of the pristine and the ion implanted samples.